PAPER

Efficient band alignment for Zn$_x$Cd$_{1-x}$Se QD-sensitized TiO$_2$ solar cells

Lin Yang,[ab] Ru Zhou,[a] Jolin Lan,[a] Qifeng Zhang,[a] Guozhong Cao[*a] and Jianguo Zhu[b]

Zn$_x$Cd$_{1-x}$Se QDs sensitized TiO$_2$ photoelectrodes on FTO substrates have been prepared using an ion-exchange route. The lattice parameters and band gaps of such Zn$_x$Cd$_{1-x}$Se QDs were found to have linear and quadratic relationships with the Zn content (x). These TiO$_2$/Zn$_x$Cd$_{1-x}$Se films were further assembled to solar cells and demonstrated to be promising photoelectrodes for solar cells. In the fabricated QDs sensitized solar cells, QDs with the composition of $x = 0.6$ produced the highest photocurrent and photoconversion efficiency. It demonstrates that the effective band alignment of the QDs is favorable to enhance the photovoltaic performance for solar cells, by producing an efficient electron–hole separation following a band alignment.

Introduction

Due to its renewable and clean-energy characteristics, solar energy is destined to be an important energy source for the next generation. Since the significant breakthrough in dye-sensitized solar cells (DSSCs) was first reported by O'Regan and Grätzel in 1991,[1] DSSCs have attracted much attention as a low-cost alternative to conventional semiconductor heterojunction solar cells. The performance of such DSSCs depends largely on the properties of the sensitizers. Therefore, the search for and the development of new sensitizers have played decisive roles in the enhancement of the power conversion efficiency and device stability. As an alternative, semiconductor quantum dots (QDs), such as CdS,[2,3] CdTe,[4–6] PbS,[7,8] PbSe,[9,10] and InP,[11,12] have recently been extensively studied as light harvesters, to replace the molecular dyes in DSSCs, due to their unique advantages. For example, the energy band gap of QDs can be tailored by changing their size, allowing the absorption spectra to be tuned to match the spectral distribution of sunlight. In comparison with organic dye molecules, QDs have higher extinction coefficients and larger intrinsic dipole moments.[13,14] Additionally, QDs have opened up a way to utilize hot electrons to generate multiple electron–hole pairs, with a single photon, *via* the impact ionization effect.[15,16]

In spite of the advantages of QDs over organic dyes, there are relatively fewer studies devoted to QD-sensitized solar cells (QDSSCs), and their power conversion efficiencies are still lower. The poor performance of QDSSCs may be attributed to the difficulty of incorporating the QDs into a TiO$_2$ mesoporous matrix to obtain a well-covered QD monolayer on the inner surface of the TiO$_2$ electrode. The other problem one would encounter is the selection of an efficient electrolyte, in which the metal chalcogenide can run stably, without serious degradation.

An improvement of the power conversion efficiency of QDSSCs might be realized through one of the following ways: (i) an efficient method to control the crystal size and size distribution of the QDs[17,18] or (ii) optimization of the QD sensitized electrode structure, including integration of a suitable wide band gap matrix, high coverage, and band alignment of the QDs, which will be favorable to both electron transfer and collection.[19–22]

Since binary semiconductors have fixed band levels, it is difficult to find the best semiconductors to form suitable band alignment at the interface with wide band gap semiconductors. These problems can be circumvented by using ternary or quaternary semiconductors that form a solid solution (*i.e.*, an alloy) and possess a band level varying with the change of the chemical composition. However, the reports of using ternary or quaternary semiconductors to manipulate the interfacial band alignment have been scarce, so far.[23,24]

In this context, an interesting alternative to the tuning of the absorption region is the formation of alloy structures, allowing for the band gap variation by changing the composition of the QDs. Examples include alloyed Zn$_x$Cd$_{1-x}$Se QDs, the band gap of which can be varied by changing x between the values of the pure ZnSe and the pure CdSe QDs of the same size and crystal structure. To do so, we design and report an ion-exchange route to prepare TiO$_2$/Zn$_x$Cd$_{1-x}$Se electrodes with a tunable QD composition ($0 < x < 1$) and band gaps from 1.76 to 2.75 eV. These TiO$_2$/Zn$_x$Cd$_{1-x}$Se films are further demonstrated to be promising photoelectrodes for photoelectrochemical solar cells, giving a maximum power conversion efficiency of 3.70%. A

[a]*Department of Materials and Engineering, University of Washington, Seattle, Washington 98195-2120, USA. E-mail: gzcao@u.washington.edu; Fax: +1-206-543-3100; Tel: +1-206-616-9084*

[b]*College of Materials Science and Engineering, Chengdu 610064, Sichuan, P. R. China*

This journal is © The Royal Society of Chemistry 2014

J. Mater. Chem. A, 2014, **2**, 3669–3676 | 3669

comprehensive analysis was employed to examine the band gaps as a function of the Zn content (x), to enable an understanding of the composition dependence of the power conversion efficiency. On the basis of the experimental results, a possible formation mechanism involving the band alignment has been proposed in this paper.

Experimental

a. Chemicals and methods

Zinc acetate dihydrate ($Zn(AC)_2 \cdot 2H_2O$, 99.9%), cadmium nitrate tetrahydrate ($Cd(NO)_3 \cdot 4H_2O$, 98.0%), sodium borohydride ($NaBH_4$, 97.0%), and selenium powder (Se, 97.0%) were used as starting materials. All the reagents used were of analytical purity and were used directly, without further purification.

Mesoscopic TiO_2 films were prepared by the coating of TiO_2 paste (Degussa P25) on a piece of ultrasonically cleaned F-doped tin oxide (FTO, about 8 Ω per sq., Solaronix SA) substrate, followed by sintering at 500 °C, for 30 min, to improve the crystallinity and remove impurities. The thickness of the TiO_2 film, measured from the cross sectional image from a scanning electron microscope, was about 12.0 μm. A Se source solution (NaHSe) was first prepared by dissolving 5 mmol of $NaBH_4$ and 2.5 mmol of Se in deionized water, under a nitrogen atmosphere. The chemical bath deposition (CBD) process involved dipping the TiO_2 film in a 0.05 M $Zn(AC)_2$ aqueous solution for 2 min, rinsing it with deionized water, and then dipping it for another 2 min in a 0.05 M NaHSe aqueous solution, and rinsing it again with deionized water. The two-step dipping procedure is considered as one CBD cycle. The incorporated amount of ZnSe can be increased by repeating the assembly cycle.

$TiO_2/Zn_xCd_{1-x}Se$ with different QDs compositions were obtained by the immersion of the $TiO_2/ZnSe$ template into a Cd^{2+} source solution (0.05 M $Cd(NO)_3$ aqueous solution) at different temperatures (RT, 30, 40, 60, and 80 °C) for 3 h. In this process, the cation of Cd^{2+} substitutes the Zn^{2+} in the ZnSe, to form ZnCdSe, with different atomic ratios of Cd to Zn. Different ratios of Cd/Zn in the ZnCdSe QDs can be achieved by controlling the reaction temperature of the $TiO_2/ZnSe$ electrode with the Cd^{2+} ions.

For photovoltaic applications, the as-prepared $TiO_2/Zn_xCd_{1-x}Se$ electrodes were modified with ZnS by twice dipping alternately into 0.1 M Zn ($CH_3COO)_2$ and 0.1 M Na_2S aqueous solutions for 1 min each, rinsing with deionized water between the dips. Nanostructured Cu_2S counter-electrodes were prepared by immersing a brass sheet in a HCl solution (37 wt%) at 80 °C for 40 min and subsequently dipping it into a polysulfide electrolyte (1.0 M S and 1.0 M Na_2S in deionized water) for 5 min. The active area of the cell was 0.36 cm^2.

b. Characterization

The as-prepared samples were characterized by X-ray diffraction (XRD) using a Bruker F8 diffractometer with Cu K α radiation. Scanning electron microscopy (SEM) and transmission electron microscopy (TEM) were carried out with a JSM-7000 SEM and a Tecnai G2 F20 TEM, respectively. The compositional analysis

and elemental mapping of the as-prepared sample were performed with an energy-dispersive X-ray spectroscopy (EDX) system, an accessory of the SEM. The Raman measurements were conducted to further confirm the composition with a Hololab 5000 laser Raman microscope, equipped with a 768 nm argon ion laser of 2 mm spot size for the excitation. The absorption spectra were recorded with a UV-vis spectrophotometer (Perkin Elmer Lambda 900). The photocurrent-voltage (J–V) curves were measured under an illumination of a solar simulator (HP 4155A) at one sun (AM1.5, 100 mW cm^{-2}). The electrochemical impedance spectroscopy (EIS) measurements were performed on a Solartron 1287A, coupling with the Solartron 1260 FRA/impedance analyzer in the dark, by applying a bias voltage of −0.6 V, from 10^{-1} to 10^5 Hz, to investigate the charge transfer dynamics of the QDSSCs.

Results and discussion

A typical high-resolution TEM image of the $TiO_2/Zn_{0.6}Cd_{0.4}Se$ is shown in Fig. 1a. The fringe spacing of 0.352 nm in the single-crystalline core closely matches the interplanar spacing of the (101) plane of tetragonal TiO_2,[25] while the lattice spacing of 0.342 nm in the polycrystalline particle closely matches the interplanar spacing of the (111) planes of cubic $Zn_{0.6}Cd_{0.4}Se$ QDs.

The compositional EDX analysis of the $TiO_2/Zn_xCd_{1-x}Se$ films was carried out over a sample area of 6 μm^2. The synthesis conditions and the corresponding QDs, with different compositions, are listed in Table 1. As illustrated in Fig. 1, the EDX
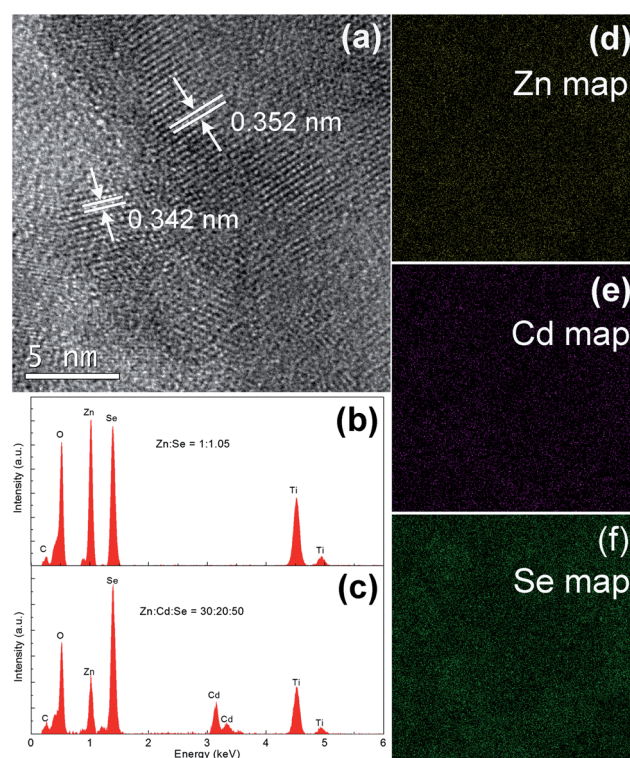
Fig. 1 (a) HRTEM image of $TiO_2/Zn_{0.6}Cd_{0.4}Se$ QDs; EDX spectra of ZnSe (b) and $Zn_{0.6}Cd_{0.4}Se$ (c) QDs; (d–f) element distribution maps of Zn, Cd and Se elements in $Zn_{0.6}Cd_{0.4}Se$ QDs.

3670 | J. Mater. Chem. A, 2014, 2, 3669–3676

This journal is © The Royal Society of Chemistry 2014

Table 1 Composition of $Zn_xCd_{1-x}Se$ QDs synthesized in the different conditions

Synthesis condition	Zn/(Zn + Cd) (%)	Composition of QDs	No.
N/A	100	ZnSe	A
RT, 3 h	70	$Zn_{0.7}Cd_{0.3}Se$	B
30 °C, 3 h	60	$Zn_{0.6}Cd_{0.4}Se$	C
40 °C, 3 h	40	$Zn_{0.4}Cd_{0.6}Se$	D
60 °C, 3 h	25	$Zn_{0.25}Cd_{0.75}Se$	E
80 °C, 3 h	8	$Zn_{0.08}Cd_{0.92}Se$	F

composition mapping confirms the presence and homogeneous distribution of the Zn, Cd and Se elements in all the samples with different atomic ratios investigated in the present study. With regard to the EDX spectrum in Fig. 1b, the atomic ratio of Zn to Se is calculated to be about 1 : 1.05 for the TiO_2/ZnSe. The deviation from a stoichiometric ratio of ZnSe is mainly caused by the oxidation of Se^{2-} on the surface of the nanoparticles into amorphous Se, in the air. After introduction of the Cd cations into the ZnSe (Fig. 1c), it indicates that the QDs consist of zinc, cadmium, and selenium, with an atomic ratio of 30 : 20 : 50. Fig. 1d–f are, respectively, the corresponding Zn, Cd and Se EDX elemental mappings, revealing that Zn, Cd and Se are homogeneously distributed throughout the films.

The XRD data reveal that $Zn_xCd_{1-x}Se$ QDs adopt a blende structure, of the ternary nanocrystals, over all the compositions (Fig. 2a). The line XRD spectra correspond to bulk ZnSe (bottom) and bulk CdSe (top), respectively. The characteristic XRD patterns of the $Zn_xCd_{1-x}Se$ QDs exhibit three prominent peaks, which are indexed to the (111), (220), and (311) planes, respectively. It is worth noting that the diffraction peaks of the $Zn_xCd_{1-x}Se$ QDs are gradually shifted to the larger angles, as the Zn content increases (*i.e.*, the increase in x). The continuous peak shift may also rule out a phase separation or separated nucleation of the ZnSe or CdSe QDs.[26,27] Additionally, Fig. 2b shows the XRD patterns ($2\theta = 20–35°$) for the magnified scaled (111) peaks of $Zn_{0.6}Cd_{0.4}Se$, $Zn_{0.4}Cd_{0.6}Se$ and $Zn_{0.25}Cd_{0.75}Se$. The broad and asymmetric peak profile implies the inhomogeneous distribution of the Cd and Zn elements.[28] The asymmetric (111)
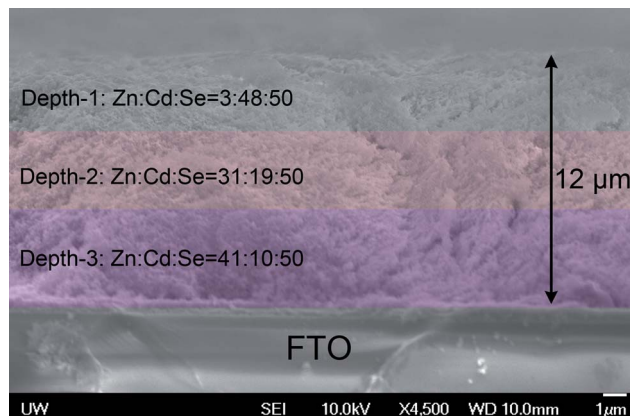
Fig. 3 Cross-sectional SEM image of TiO_2/$Zn_{0.6}Cd_{0.4}Se$ photoanode.
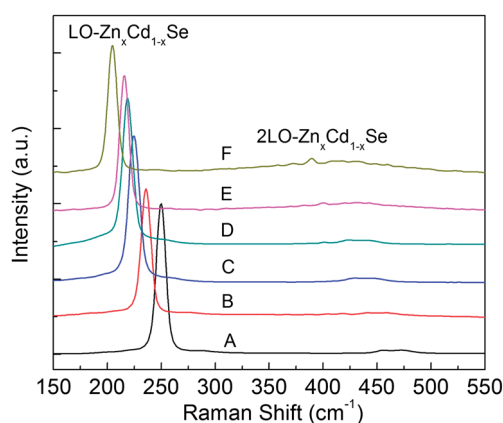
Fig. 4 Raman spectra of $Zn_xCd_{1-x}Se$ QDs with different compositions (the peaks of TiO_2 were deducted).

peak is able to be resolved into two or three bands (P_1–P_3), as shown by the dotted lines. For example, the (111) peak at $x = 0.6$ was resolved into three bands by means of the Voigt function.[29] The composition of the three components (x_i) was calculated according to Vegard's law and then the average composition was estimated by using the mean equation: $x = \sum x_i f_i$, where
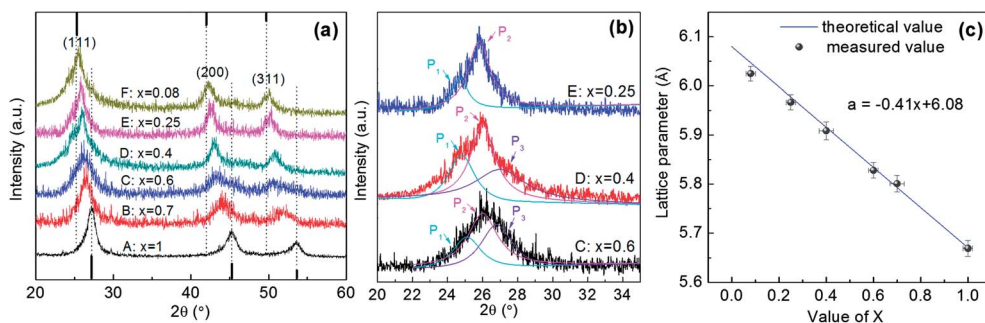
Fig. 2 (a) XRD patterns of $Zn_xCd_{1-x}Se$ QDs (x = 0.08, 0.25, 0.4, 0.6, 0.7, 1) and (b) the magnified region of $Zn_{0.6}Cd_{0.4}Se$, $Zn_{0.4}Cd_{0.6}Se$ and $Zn_{0.25}Cd_{0.75}Se$ peaks ($2\theta = 20–35$ degrees). The diffractive peaks of TiO_2 and FTO were deducted from the XRD pattern; (c) a linear relationship of the lattice parameter of $Zn_xCd_{1-x}Se$ QDs as a function of Zn mole fractions, which is measured from the XRD patterns (spherical data points) and calculated from Vegard's law (solid line).
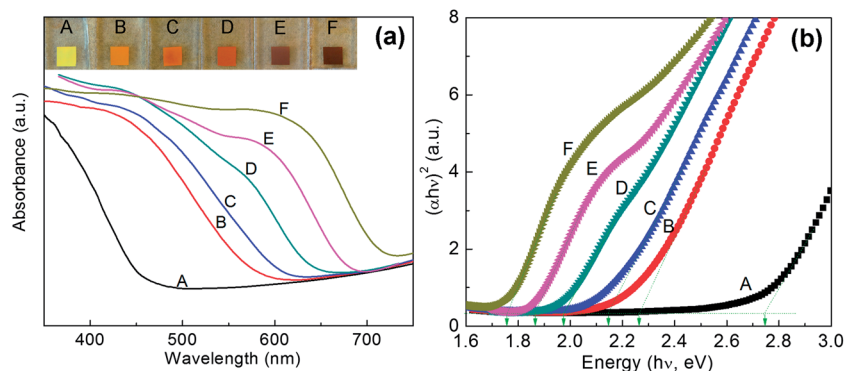
This journal is © The Royal Society of Chemistry 2014

J. Mater. Chem. A, 2014, **2**, 3669–3676 | **3671**

Fig. 5 (a) UV-visible absorption spectra of TiO$_2$/Zn$_x$Cd$_{1-x}$Se films and (b) calculation of optical band gaps from the UV-vis absorption spectra.

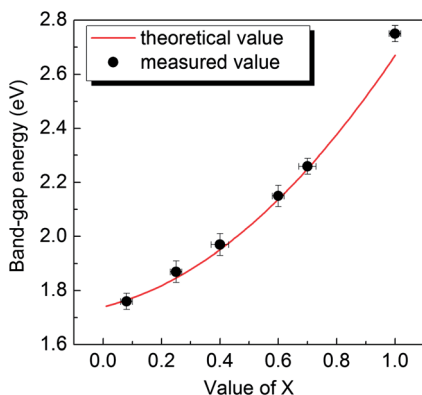**Fig. 6** A quadratic relationship of the band gaps of the ternary Zn$_x$Cd$_{1-x}$Se QDs as a function of the Zn/(Zn + Cd) molar ratio.

Table 2 Photovoltaic parameters obtained from the J–V curves using TiO$_2$/Zn$_x$Cd$_{1-x}$Se QDs as electrodes

No.	Composition of QDs	V_{OC} (V)	J_{SC} (mA cm^{-2})	FF	Efficiency (%)
A	ZnSe	0.40	3.47	0.42	0.59
B	Zn$_{0.7}$Cd$_{0.3}$Se	0.57	8.72	0.47	2.31
C	Zn$_{0.6}$Cd$_{0.4}$Se	0.57	12.80	0.51	3.70
D	Zn$_{0.4}$Cd$_{0.6}$Se	0.57	10.68	0.49	2.97
E	Zn$_{0.25}$Cd$_{0.75}$Se	0.55	6.15	0.47	1.59
F	Zn$_{0.08}$Cd$_{0.92}$Se	0.55	5.35	0.47	1.38

f_i is the area fraction of the resolved bands. It has $x_i = 0.05, f_1 = 0.18$; $x_i = 0.6, f_1 = 0.46$ and $x_i = 0.8, f_1 = 0.36$, so the average composition ($x = 0.6$) is the same as that determined from the position of the unresolved peaks. This analysis indicates that the Zn-rich and Cd-rich composition layers explicitly coexist.

We consider that the mechanism for the formation of three different phases is possibly that there exists a composition gradient due to the diffusion of Cd^{2+} from the surface to the

bottom of the TiO$_2$ film, *i.e.*, a fast formation of QDs in the upper section and prevention of the precursor solution from entering into the deep pores. During the ion-exchange process, the TiO$_2$/ZnSe film was immersed into the Cd^{2+} precursor solution, and then Cd^{2+} substituted some of the Zn^{2+}. Some Zn$_x$Cd$_{1-x}$Se QDs were formed quickly and blocked most of the pores in the upper section of the film, which prevented the Cd^{2+} precursor solution from infusing into the deep pores. So, it was impossible to completely replace it with Zn^{2+} in the deep pores along the transverse of the TiO$_2$ film. To further support our proposed mechanism, SEM of the sample transverse and EDX calculation in the different depth sections of the photoanode film was employed, as shown in Fig. 3. As also mentioned above,
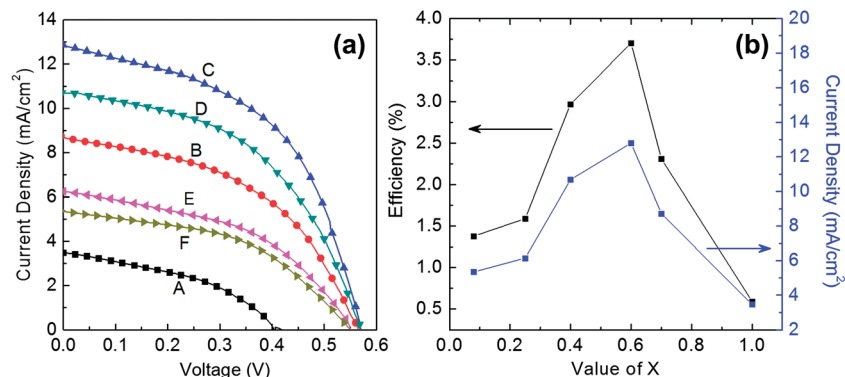

Fig. 7 (a) Current density–voltage (J–V) characteristics of the solar cells using TiO$_2$/Zn$_x$Cd$_{1-x}$Se as the photoelectrode; (b) dependence of J_{SC} and η on the composition of Zn$_x$Cd$_{1-x}$Se QDs.

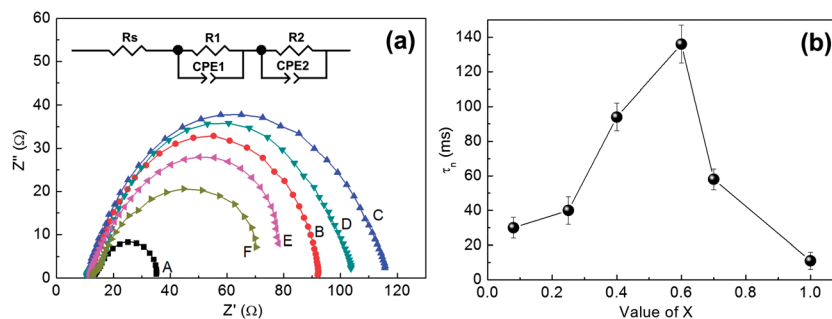**Fig. 8** (a) EIS spectra and (b) electron lifetime of QDSSCs based on $TiO_2/Zn_xCd_{1-x}Se$ photoanode measured in the dark at -0.6 V bias. The inset in (a) illustrates the equivalent circuit simulated to fit the impedance spectroscopy. R_1 and CPE_1 represent the charge transfer resistance and capacitance at electrolyte–counter electrode interface, respectively; while R_2 and CPE_2 represent the recombination resistance and capacitance at the photoanode/electrolyte interface, respectively.

the content of Cd decreases from the surface to the bottom of the film. The Zn-rich and Cd-rich compositions concentrate on the upper and the lower depth sections, respectively. The atomic ratios of Zn : Cd : Se are also in accordance with the compositions resolved from the XRD patterns in terms of Vegard's law.

Further structural evidence can be tracked by analyzing the average change in the lattice parameters by XRD measurements, and then Vegard's law can be applied to check the compositional homogeneity in the semiconductor nanocrystals. According to Vegard's law,[30] the alloys should show a linear relationship between the crystal lattice parameters and average composition. As shown in Fig. 2c, the lattice parameter measured from the XRD patterns of the $Zn_xCd_{1-x}Se$ QDs exhibits a nearly linear relationship with the Zn content. A progressive decrease in the lattice parameter from 6.025 to 5.967, 5.909, 5.828, 5.801 and 5.669 Å is observed as the Zn content (x) increases (from 0.08 to 0.25, 0.4, 0.6, 0.7 and 1) owing to the smaller ionic radius of Zn, relative to that of Cd. This trend is consistent with Vegard's law and thus indicates a homogeneous alloy structure.

To further confirm the nominal composition of the $Zn_xCd_{1-x}Se$ sensitized TiO_2 film, Raman measurements were carried out, and the results are shown in Fig. 4. The Raman peaks of the first-order longitudinal optical phonon mode (LO) in the $TiO_2/Zn_xCd_{1-x}Se$ film show a systematic decrease from 250 cm^{-1} for ZnSe, to 236 cm^{-1} for $Zn_{0.7}Cd_{0.3}Se$, 225 cm^{-1} for $Zn_{0.6}Cd_{0.4}Se$, 219 cm^{-1} for $Zn_{0.4}Cd_{0.6}Se$, 216 cm^{-1} for $Zn_{0.25}Cd_{0.75}Se$, and 205 cm^{-1} for $Zn_{0.08}Cd_{0.92}Se$, with increasing Cd content. This continuous shift further confirms that the as-

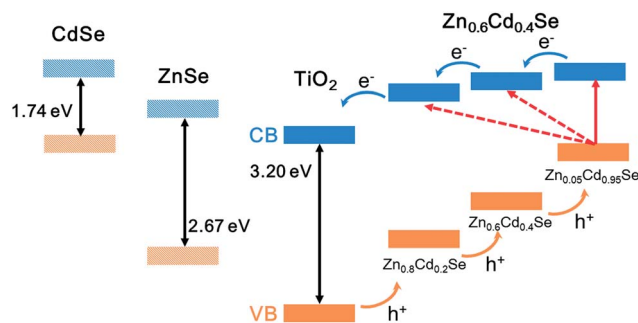**Fig. 9** A schematic diagram for the band alignment model in $Zn_{0.6}Cd_{0.4}Se$ QDs sensitized TiO_2 photoelectrode.

prepared QDs are nominally a homogeneous ternary alloy of tunable compositions, instead of a mixture of ZnSe and CdSe nanocrystals.[26,31]

Fig. 5a shows the UV-vis absorption spectra of the $TiO_2/Zn_xCd_{1-x}Se$ films. The $TiO_2/ZnSe$ film absorbs only over the UV region at a wavelength shorter than 450 nm. An expanded absorption edge in the visible light region is demonstrated upon the formation of the $Zn_xCd_{1-x}Se$ QDs, which is consistent with their color change from yellow for the $TiO_2/ZnSe$ films, to bright red for the $TiO_2/Zn_{0.6}Cd_{0.4}Se$ films and then to dark red for the $TiO_2/Zn_{0.08}Cd_{0.92}Se$ films (the inset of Fig. 5a). The absorption shoulder of the $Zn_xCd_{1-x}Se$ QDs sensitized TiO_2 film is red-shifted with decreasing Zn content, suggesting that the decrease of the optical band gap stems from the stoichiometry variation in the ternary alloy semiconductors. Thus, the Cd-rich

Table 3 Simulated values of resistance (R), capacitance (CPE) and electron lifetime (τ_n) of EIS spectra calculated by equivalent circuit

No.	Composition of QDs	R_S (Ω)	R_1 (Ω)	CPE_1 (μF)	R_2 (Ω)	CPE_2 (μF)	τ_n (ms)
A	ZnSe	12.7	2.6	273	22.1	503	11
B	$Zn_{0.7}Cd_{0.3}Se$	11.4	0.5	687	80.7	715	58
C	$Zn_{0.6}Cd_{0.4}Se$	10.7	0.6	556	104.9	1296	136
D	$Zn_{0.4}Cd_{0.6}Se$	10.9	2.2	291	93.5	1006	94
E	$Zn_{0.25}Cd_{0.75}Se$	12.1	1.3	500	65.8	604	40
F	$Zn_{0.08}Cd_{0.92}Se$	12.6	2.7	367	57.4	526	30

This journal is © The Royal Society of Chemistry 2014

J. Mater. Chem. A, 2014, **2**, 3669–3676 | **3673**

composition of the QDs decreases the band gap, to amplify the photon absorption at the longer wavelength. Herein, the raising baseline at a longer wavelength is mainly due to the abnormality of the reference sample. The optical band gaps of each sample were evaluated by Tauc's diagrams[32] plotting the $(\alpha h\nu)^2$ absorption functions against the photon energy, which is possible in these direct band gap semiconductors. The band gaps of the $Zn_xCd_{1-x}Se$ QDs were estimated from the intersection points of two fitting lines, the saturation and incline lines, as shown in Fig. 5b (marked in cyan). The plots are presented for $Zn_xCd_{1-x}Se$ with x values of 1, 0.70, 0.60, 0.40, 0.25 and 0.08 to illustrate estimation of the band gaps with values of 2.75, 2.26, 2.15, 1.97, 1.87 and 1.76 eV, correspondingly. It should be noted, especially, that there is possibly a mixture of two or three absorption spectra, particular for samples D and E. This observation is consistent with the XRD results, as discussed earlier.

While the lattice parameters of the ternary $Zn_xCd_{1-x}Se$ QDs change linearly with the composition, the band gaps often vary non-linearly. To a first approximation, the non-linearity can be expressed by a quadratic function.[33] As anticipated, the band gap energy (E_g) of $Zn_xCd_{1-x}Se$ nanocrystals is between those of ZnSe and CdSe. The dependence of E_g on the composition (x) of the $Zn_xCd_{1-x}Se$ QDs could be been described previously, using eqn (1) as follows, where b refers to the bowing parameter (for $Zn_xCd_{1-x}Se$, $b = 0.67$),[31] describing the extent of non-linearity.

$$E_g(x) = E_g^{ZnSe}(x) + E_g^{CdSe}(1 - x) - bx(1 - x) \qquad (1)$$

By considering the bulk band gap of ZnSe (2.67 eV) and that of CdSe (1.74 eV), this equation could be simplified as

$$E_g(x) = 2.67(x) + 1.74(1 - x) - 0.67x(1 - x) = 067x^2 + 0.26x + 1.74 \qquad (2)$$

Fig. 6 corresponds to the plot of the band gap energy (E_g) as a function of x, showing a significant deviation from linearity. The theoretical values, calculated from eqn (2), are represented by the solid line. The measured values, estimated from the typical UV-vis spectra, are shown as solid circle points, with the error bars on the y axis reflecting the mean deviation of the band gap energy. We can see that the measured values of E_g show a remarkable agreement with the calculated curve, based on eqn (2).

Fig. 7a shows the current density–voltage (J–V) characteristics of the solar cells, configured using the samples as photoanodes, a Cu_2S counter electrode, and an electrolyte based on a 1 M Na_2S and 1 M S aqueous solution. The key performance parameters of the various cells are summarized in Table 2 and Fig. 7b. The solar cell based on TiO_2/ZnSe (curve A) gives a short-circuit current density (J_{SC}) of 3.47 mA cm^{-2}, an open circuit voltage (V_{OC}) of 0.40 V, and a fill factor (FF) of 0.42, yielding a power conversion efficiency (η) of 0.59%. With increasing Cd content in the $Zn_xCd_{1-x}Se$ QDs, both J_{SC} and η drastically increase to 8.72 mA cm^{-2} and 2.31% for TiO_2/$Zn_{0.7}Cd_{0.3}Se$ (curve B), and further to 12.80 mA cm^{-2} and 3.70% for TiO_2/$Zn_{0.6}Cd_{0.4}Se$ (curve C), and then decrease to 5.35 mA cm^{-2} and

1.38% for TiO_2/$Zn_{0.08}Cd_{0.92}Se$ (curve F) while their V_{OC} remains at the value of ~0.56 V.

Fig. 8a shows the Nyquist curves of the EIS results, containing typically two semicircles, which are fitted by the equivalent circuit (the inset in Fig. 8a) with the fitted values listed in Table 3, where R_S is the substrate resistance, R_1 and R_2 can be estimated, respectively, from the real impedance component (Z') of the high-frequency semicircles (the small semicircle) and the low-frequency semicircles (the larger semicircle), and then the electron lifetime can be estimated by $\tau_n = R_2 \times CPE_2$.[34,35] At the counter electrode–electrolyte interface, the recombination resistance R_1 exhibits no apparent differences among these five QDSSCs, while the same counter electrode and electrolyte are used in our experiments. The simulated data of the charge transfer resistance R_2, for the electron transfer process at the TiO_2/$Zn_{0.6}Cd_{0.4}Se$ QDs–electrolyte interface is larger than that of the QDSSCs with the other compositions, ascribed to the reduced interfacial recombination, contributing to the obvious improvement in J_{SC} and FF. Fig. 8b shows the variation in the electron lifetime with the composition of the QDs. The long-lived charge carriers imply a low charge recombination, so as to result in a high performance of the QDSSCs. Therefore, in our case, $Zn_{0.6}Cd_{0.4}Se$ is indicated to remain the highest value of τ_n, ~136 ms. However, the electron lifetime drops to ~30 ms when TiO_2/$Zn_{0.08}Cd_{0.92}Se$ was used as the photoelectrode. According to the EIS results and the J–V characteristics, the most appropriate composition for a TiO_2/ $Zn_xCd_{1-x}Se$ photoanode film should be $x = 0.6$, which gives the longest electron lifetime and highest efficiency.

It is well-known that in the photosensitizing architecture, a suitable alignment of the energy levels is more significant for an efficient electron injection from a photo-excited sensitizer to a wide band gap semiconductor.[36,37] On comparison of the data of the band edges reported in the literature,[38,39] it is noteworthy that ZnSe has a higher conduction band edge, with respect to that of TiO_2, which is advantageous to the injection of excited electrons from ZnSe. However, the band gap of ZnSe (2.67 eV in bulk) limits its absorption range approximately below the wavelength of 480 nm. On the contrary, although CdSe has a wider absorption range (below 730 nm), the electron injection efficiency is less, because its conduction band edge is located below that of TiO_2. When TiO_2, ZnSe and CdSe are connected together, the energy levels difference between ZnSe and CdSe causes the electrons to flow from ZnSe (higher level) to CdSe (lower level). Such an electron transfer is known as the Fermi level alignment. The redistribution of the electrons between ZnSe and CdSe is supposed to trigger a downward and upward shift of the band edges, respectively, for ZnSe and CdSe. So, the insertion of ZnSe between TiO_2 and CdSe could provide a large driving force for the injection of photoexcited electrons to the TiO_2, by elevating the conduction band edge of CdSe. This result sustains the previous inference of band alignment (Fermi-level alignment), proposed to explain the high performance of the CdS and CdSe co-sensitized photoelectrode.[40–42] Herein, we suggest a band alignment model, as illustrated in Fig. 9. We simply suppose that the $Zn_{0.6}Cd_{0.4}Se$ QDs contain $x = 0.05$, 0.6 and 0.8. As a comparison, it is observed that the band positions of these three

3674 | J. Mater. Chem. A, 2014, 2, 3669–3676

This journal is © The Royal Society of Chemistry 2014

compositions locate at an intermediate position between the bands of pure ZnSe and pure CdSe. If the band position of the Cd-rich layer (*i.e.*, the QDs layer with a lower *x* value) shifts upward, the layer could produce photoelectrons upon visible light absorption, and then the photoelectrons will be transferred to the lower energy conduction band (CB) of the Zn-richer layer. A possible transition from the valence bond (VB) of the Cd-rich layer to the CB of the Zn-rich layer decreases the band gap to amplify the photon absorption at the longer wavelength (as marked by the dotted arrows). Therefore, the inner layer can provide a driving force for the injection of photoexcited electrons from the outer layer to the TiO$_2$ film, by creating an optimized band alignment, which is favorable to the transport of both electrons and holes across the photoelectrode. We conclude that such a layered structure induces a synergistic effect, which increases the photon absorption and favors charge transfer, resulting in an enhancement performance of the solar cells.

Conclusions

Zn$_x$Cd$_{1-x}$Se QDs were synthesized through a simple and facile ion-exchange method after the formation of CdSe QDs and were used to sensitize mesoporous TiO$_2$ films as photoelectrodes for QD-sensitized solar cells. It was found that the Zn$_x$Cd$_{1-x}$Se QDs adopt a blende structure of the ternary nanocrystals over all the compositions and the ternary Zn$_x$Cd$_{1-x}$Se layers with tunable band gap properties extend the band-edge of the optical light absorption from 450 to 700 nm, compared to the binary ZnSe layers. The Cd-rich and Zn-rich composition layers explicitly coexist in Zn$_{0.6}$Cd$_{0.4}$Se QDs, owing to a diffusion of Cd cations. This quantitative investigation of the electronic energy levels at the TiO$_2$ and Zn$_{0.6}$Cd$_{0.4}$Se interfaces indicates that a proper band alignment favors the enhanced photovoltaic energy conversion. A suitable adjustment for the band gap of ternary sensitizers contributes to a high photovoltaic performance for TiO$_2$/Zn$_x$Cd$_{1-x}$Se, with a maximum power conversion efficiency up to 3.70%, by producing an efficient electron–hole separation following a band alignment. The charge separation is obtained by electron transfer from the excited sites of Zn$_x$Cd$_{1-x}$Se to TiO$_2$ and compensation of the holes left on the sensitizer layer by an electrolyte donor. It would be expected to enhance the photovoltaic performance of QDSSCs significantly, through the present ion-exchange method.

Acknowledgements

References

1 B. O'Regan and M. Grätzel, *Nature*, 1991, **353**, 737–740.

2 W. T. Sun, Y. Yu, H. Y. Pan, X. F. Gao, Q. Chen and L. M. Peng, *J. Am. Chem. Soc.*, 2008, **130**, 1124–1125.

3 L. Li, X. C. Yang, J. J. Gao, H. N. Tian, J. Z. Zhao, A. Hagfeldt and L. C. Sun, *J. Am. Chem. Soc.*, 2011, **133**, 8458–8460.

4 J. A. Seabold, K. Shankar, R. H. T. Wilke, M. Paulose, O. K. Varghese, C. A. Grimes and K. S. Choi, *Chem. Mater.*, 2008, **20**, 5266–5273.

5 J. H. Bang and P. V. Kamat, *ACS Nano*, 2009, **3**, 1467–1476.

6 J. A. Seabold, K. Shankar, R. H. T. Wilke, M. Paulose, O. K. Varghese, C. A. Grimes and K.-S. Choi, *Chem. Mater.*, 2008, **20**, 5266–5273.

7 Z. Tachan, M. Shalom, I. Hod, S. Rühle, S. Tirosh and A. Zaban, *J. Phys. Chem. C*, 2011, **115**, 6162–6166.

8 L. Etgar, T. Moehl, S. Gabriel, S. G. Hickey, A. Eychmüller and M. Grätzel, *ACS Nano*, 2012, **6**, 3092–3099.

9 K. S. Leschkies, T. J. Beatty, M. S. Kang, D. J. Norris and E. S. Aydi, *ACS Nano*, 2009, **3**, 3638–3648.

10 J. J. Choi, Y.-F. Lim, M. B. Santiago-Berrios, M. Oh, B.-R. Hyun, L. F. Sun, A. C. Bartnik, A. Goedhart, G. G. Malliaras, H. D. Abruña, F. W. Wise and T. Hanrath, *Nano Lett.*, 2009, **9**, 3749–3755.

11 A. Zaban, O. I. Mićić, B. A. Gregg and A. J. Nozik, *Langmuir*, 1998, **14**, 3153–3156.

12 J. M. Nedeljković, O. I. Mićić, S. P. Ahrenkiel, A. Miedaner and A. J. Nozik, *J. Am. Chem. Soc.*, 2004, **126**, 2632–2639.

13 H. Tada, M. Fujishima and H. Kobayashi, *Chem. Soc. Rev.*, 2011, **40**, 4232–4243.

14 W. W. Yu, L. H. Qu, W. Z. Guo and X. G. Peng, *Chem. Mater.*, 2003, **15**, 2854–2860.

15 C.-H. Chang and Y.-L. Lee, *Appl. Phys. Lett.*, 2007, **91**, 053503.

16 Y.-L. Lee, B.-M. Huang and H.-T. Chien, *Chem. Mater.*, 2008, **20**, 6903–6905.

17 H. Y. Fu, S.-W. Tsang, Y. G. Zhang, J. Y. Ouyang, J. P. Lu, K. Yu and Y. Tao, *Chem. Mater.*, 2011, **23**, 1805–1810.

18 J. J. Tian, R. Gao, Q. F. Zhang, S. G. Zhang, Y. W. Li, J. Lan, X. H. Qu and G. Z. Cao, *J. Phys. Chem. C*, 2012, **116**, 18655–18662.

19 Y.-L. Lee, C.-F. Chi and S.-Y. Liau, *Chem. Mater.*, 2010, **22**, 922–927.

20 J. C. Ni, Z. M. Wu, X. G. Lin, J. J. Zheng, S. P. Li, J. Li and J. Y. Kang, *J. Mater. Res.*, 2012, **27**, 730–733.

21 S. Cho, J.-W. Jang, J. Kim, J. S. Lee, W. Choi and K.-H. Lee, *Langmuir*, 2011, **27**, 10243–10250.

22 H. J. Lee, J. Bang Park, J. S. Kim and S.-M. Park, *Chem. Mater.*, 2010, **22**, 5636–5643.

23 Z. H. Chen, S. Y. Yeung, H. Li, J. C. Qian, W. J. Zhang, Y. Y. Li and I. Bello, *Nanoscale*, 2012, **4**, 3154–3161.

24 C.-T. Yuan, Y.-G. Wang, K.-Y. Huang, T.-Y. Chen, P. Yu, J. Tang, A. Sitt, U. Banin and O. Millo, *ACS Nano*, 2012, **6**, 176–182.

25 J. Zhang, M. J. Li, Z. C. Feng, J. Chen and C. Li, *J. Phys. Chem. B*, 2006, **110**, 927–935.

26 X. H. Zhong, Y. Y. Feng, W. Knoll and M. Y. Han, *J. Am. Chem. Soc.*, 2003, **125**, 13559–13563.

27 Z. T. Deng, F. L. Lie, S. Y. Shen, I. Ghosh, M. Mansuripur and A. J. Muscat, *Langmuir*, 2009, **25**, 434–442.

28 Y. Myung, J. H. Kang, J. W. Choi, M. D. Jang and J. Park, *J. Mater. Chem.*, 2012, **22**, 2157–2165.

This journal is © The Royal Society of Chemistry 2014

J. Mater. Chem. A, 2014, **2**, 3669–3676 | 3675

29 G. Perna, V. Capozzi, M. C. Plantamura, A. Minafra, S. Orlando and V. Marotta, *Eur. Phys. J. B*, 2002, **29**, 541–545.

30 K. M. Hanif, R. W. Meulenberg and G. F. Strouse, *J. Am. Chem. Soc.*, 2002, **124**, 11495–11502.

31 J. Xu, X. Yang, H. K. Wang, X. Chen, C. Y. Luan, Z. X. Xu, Z. Z. Lu, V. A. L. Roy, W. J. Zhang and C.-S. Lee, *Nano Lett.*, 2011, **11**, 4138–4143.

32 S. B. Bubenhofer, C. M. Schumacher, F. M. Koehler, N. A. Luechinger, R. N. Grass and W. J. Stark, *J. Phys. Chem. C*, 2012, **116**, 16264–16270.

33 S. A. Santangelo, E. A. Hinds, V. A. Vlaskin, P. I. Archer and D. R. Gamelin, *J. Am. Chem. Soc.*, 2007, **129**, 3973–3978.

34 X. Y. Yu, J. Y. Liao, K. Q. Qiu, D. B. Kuang and C. Y. Su, *ACS Nano*, 2011, **5**, 9494–9500.

35 I. Mora-Seró, S. Giménez, F. Fabregat-Santiago, R. Gómez, Q. Shen, T. Toyoda and J. Bisquert, *Acc. Chem. Res.*, 2009, **42**, 1848–1857.

36 J. Xu, X. Yang, Q. D. Yang, T. L. Wong, S.-T. Lee, W. J. Zhang and C.-S. Lee, *J. Mater. Chem.*, 2012, **22**, 13374–13379.

37 P. V. Kamat, *J. Phys. Chem. Lett.*, 2010, **1**, 3147–3148.

38 M. Grätzel, *Nature*, 2001, **414**, 338–344.

39 P. Reiss, M. Protière and L. Li, *Small*, 2009, **5**, 154–168.

40 Y.-L. Lee, C.-F. Chi and S.-Y. Liau, *Chem. Mater.*, 2010, **22**, 922–927.

41 X. F. Gao, W. T. Sun, G. Ai and L. M. Peng, *Appl. Phys. Lett.*, 2010, **96**, 153104.

42 J. Chen, J. Wu, W. Lei, J. L. Song, W. Q. Deng and X. W. Sun, *Appl. Surf. Sci.*, 2010, **256**, 7438–7441.